Suppression of nano-absorbing precursors and damage mechanism in optical coatings for 3ω mirrors

Hu Wang,[1,2] Hongji Qi,[1,*] Weili Zhang,[1] Jian Sun,[1] Yingjie Chai,[1,2] Feifei Tu,[1,2] Jiaoling Zhao,[1,2] Zhen Yu,[1,2] Bin Wang,[1,2] Meiping Zhu,[1] Kui Yi,[1] and Jianda Shao[1,3]

[1]Key Laboratory of Materials for High Power Laser, Shanghai Institute of Optics and Fine Mechanics, No. 390 Qinghe Road, Jiading District, Shanghai 201800, China
[2]University of Chinese Academy of Sciences, Beijing 100049, China
[3]e-mail: jdshao@mail.shcnc.ac.cn
*Corresponding author: qhj@siom.ac.cn

Damage precursors in the 3ω (351 nm) mirror for a high-power laser system are investigated as well as the relevant damage mechanisms. The precursors are classified into two ensembles according to the different laser resistance and damage features. The former is nano-absorbing precursors, which are sensitive to the standing wave electric field and vulnerable to the laser irradiation. The latter is submicrometer nodular defects, which have higher laser resistance and are sensitive to the adhesion strength between the fluoride coatings and oxide coatings. The damage due to nano-absorbing precursors is efficiently suppressed with the *double stack* design that screens the electric field in the oxides. Currently, the nodular seed is major originating from the Al_2O_3/SiO_2 stack. Even for the same defect type and mirror, the final damage features are dependent on the local mechanical properties at the irradiation location. The investigations of the damage mechanisms provide a direction to further improve the laser-induced damage threshold of the 3ω mirror.   © 2016 Optical Society of America

Harmonic separation is a crucial process to prevent the residual 1ω (1053 nm) and 2ω (527 nm) beams from impinging onto the target of high-power laser systems for inertial confinement fusion [1,2]. Comparing with the traditional wedged prism and focusing grating [3,4], the harmonic separation coatings, which are high reflective for the 3ω (351 nm) beam and high transmissive for the 1ω and 2ω beams, are relatively simple to fabricate and can arrange the 3ω laser efficiently due to the perpendicular reflection [5]. However, the poor laser-induced damage threshold (LIDT) limits their application in the megajoule system. Abundant investigations indicate that the damage initiation is much more affected by the 3ω whereas the 1ω

simply adds to the 3ω in enhancing damage growth [4,6]. Therefore, damage issues about the 3ω mirrors are the prior target to be resolved. Recently, interest in the harmonic separation coatings has been motivated again due to the high LIDT of fluoride multilayers [1,7–9]. Nevertheless, the stress-induced crazing limits the number of layer pairs (i.e., the reflectance) as well as the large size optics fabrication. While the excellent performance of Al_2O_3/SiO_2 mirrors in the UV solid-state lasers is reported [10], the double stack combining the fluorides and oxides shows both the high LIDT and reflectance and has a promising application in high-power laser systems [7,11,12]. Although the relationship between the LIDT and processing technique for UV mirrors has been widely studied, the damage mechanism on UV mirrors is very complicated and still obscure [1,7,12–14]. Understanding the fundamental damage process and defect nature of UV mirrors is beneficial to fabricate the harmonic separation coatings with a high LIDT and large size. Damage in the UV region initiated by nano-absorbing precursors has been widely recognized and abundant effort has been given to identify and eliminate the initiators [15–19]. In this work, initiators in UV mirrors are classified into nano-absorbing precursors and submicrometer nodular defects. The former is sensitive to the standing wave electric field (SWEF) and vulnerable to the laser irradiation, whereas the latter has higher laser resistance and is sensitive to the adhesion strength of the interface between the fluorides and oxides. The damage due to nano-absorbing precursors in UV mirrors is effectively suppressed and the discussion about the remained nodular defects provides a direction to further improve the LIDT of the 3ω mirrors.

Two UV high-reflective coatings are fabricated with the stack design of $Sub|6L(HL)^{20}H4L|Air$ and $Sub|6L(HL)^6 H4L(AM)^{11}|Air$, respectively. The former is denoted as the Al_2O_3/SiO_2 mirror and the latter is denoted as *double stack*. *Sub* represents the substrate, *Air* represents the air, H represents the $Al_2O_3(1.64)$, L represents the $SiO_2(1.46)$, A represents the
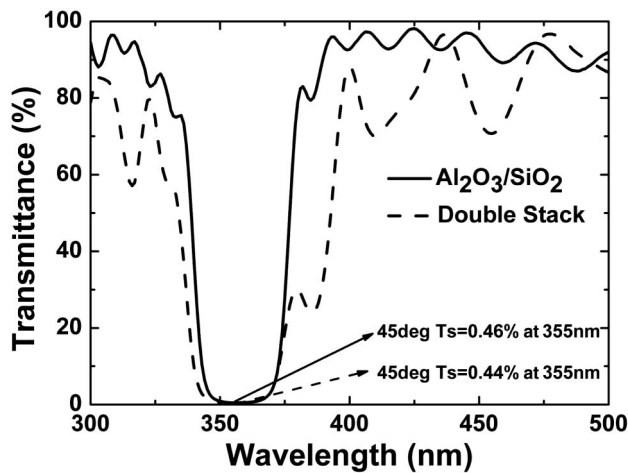
Fig. 1. Measured transmittance of the prepared mirrors.

AlF$_3$(1.35), and M represents the LaF$_3$(1.58). Each symbol represents an optical thickness of one-quarter wavelength at 400 nm. The values in parentheses depict the refractive index, and the coating conditions are detailed in our previous work [12,13]. The oxides are prepared with the electron-beam evaporation method and the fluorides are prepared with the thermal boat evaporation method. Both 3ω mirrors show excellent performance at the 45° incidence in Fig. 1. The transmittance spectra of the mirrors are measured by a PerkinElmer Lambda 1050 UV/Vis/NIR spectrometer before the damage test. The typical damage features of the UV mirrors are illustrated by the Al$_2$O$_3$/SiO$_2$ mirror, whereas the *double stack* is used to suppress the defect that is sensitive to the SWEF. As shown in Fig. 2, the electric field of the Al$_2$O$_3$/SiO$_2$ stack within the *double stack* is so small that the typical nano-absorbing precursors in the oxides will be suppressed. The stack design and the process technique have been explored and the maximal number of fluoride pairs is as high as 15 on the BK7 substrate without crazing.

The laser damage test apparatus to irradiate the two mirrors and the error analysis were both detailed in [18]. The Nd:YAG laser operating at 355 nm (8 ns pulse duration, Gaussian temporal and spatial profile) is focused on the front surface of the samples with a lens to a spot diameter 455 μm × 432 μm

($\sim e^{-2}$) at the 45° incidence in s polarization. The laser energy is controlled by the attenuator consisting of a half-wave plate and a polarizer. The damage test is conducted in the 1-on-1 mode according to ISO standard 21254 [21].

The measured damage probability versus the fluence is shown in Fig. 3(a) for both mirrors. The LIDTs of the Al$_2$O$_3$/SiO$_2$ mirror and the *double stack* are about 9.7 J/cm^2 and 15.8 J/cm^2, respectively. The higher LIDT of the *double stack* is not surprising and such a phenomenon was reported in many past works [7,11,12]. Nevertheless, little discussion on the fundamental mechanism of UV mirrors was reported other than the electric field. Damage in the UV nanosecond region is well known to be initiated by nanometer defects. To further reveal the defect information, the damage probability is fitted with the Krol method [22]. The damage probability curve for the Al$_2$O$_3$/SiO$_2$ mirror is fitted with the assumption that there are two classes of activated defects within the current fluence range. The assumption is temporarily based on the two segments as well as the best-fit results. However, more discussion with physical meaning to support such an assumption will be conducted in the following contents. The defect ensemble (solid line) of the Al$_2$O$_3$/SiO$_2$ mirror is presented with the superposition of two classes of defects (dotted line). Three basic fitting parameters including defect density (d), average threshold (T), and threshold deviation (ΔT) are used in the Krol method. The defect ensemble parameters for the best-fit curve of the Al$_2$O$_3$/SiO$_2$ mirror are: (dashed line) $d_1 = 40.0$ defects/mm^2, $T_1 = 17.0$ J/cm^2, $\Delta T_1 = 2.0$ J/cm^2; (dotted line) $d_2 = 80.0$ defects/mm^2, $T_2 = 21.0$ J/cm^2, $\Delta T_2 = 10.0$ J/cm^2. The defect ensemble parameters for the best-fit curve of the *double stack* are: $d = 80.1$ defects/mm^2, $T = 20.3$ J/cm^2, $\Delta T = 7.1$ J/cm^2. The defect ensembles calculated with fitting parameters corresponding to the best-fit curves are shown in Fig. 3(b). The defect ensemble with higher

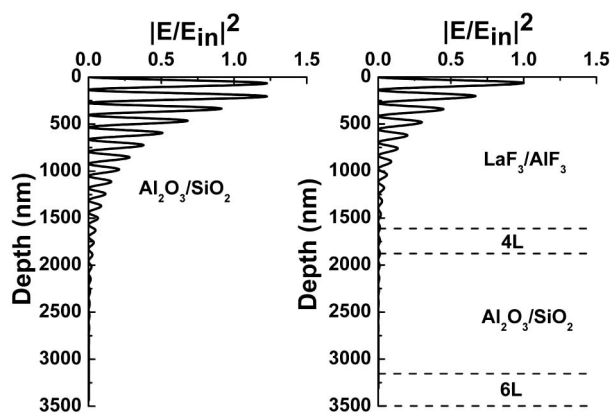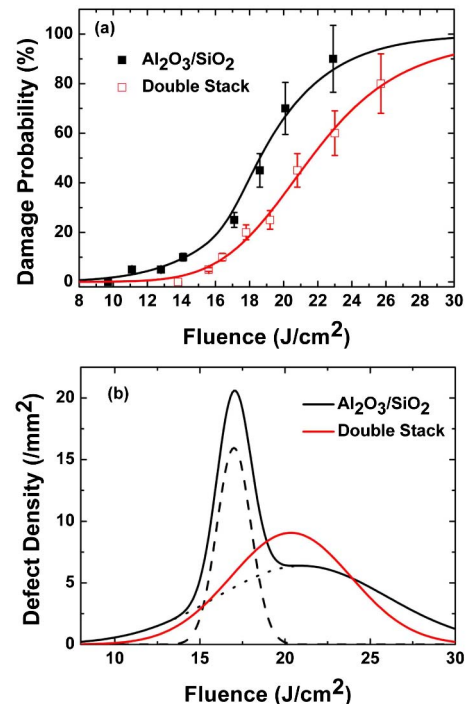**Fig. 2.** Normalized SWEF in the (left) Al$_2$O$_3$/SiO$_2$ mirror and (right) *double stack*. The SWEF is calculated as the electric field theory of Macleod [20].

Fig. 3. (a) Damage probability and (b) defect ensemble versus the fluence.

LIDT is very close to the defect ensemble of the *double stack*, which indicates the same damage type. Therefore we can infer that the defect ensemble with lower LIDT is sensitive to the SWEF and suppressed by the *double stack* design, while the defect ensemble with higher LIDT does not behave so and is more like the structural defect that breaks the SWEF. Moreover, the nanometer defects within the fluorides are not the major concern under current laser fluence since the new defect type is not observed within the current fluence range.

To further reveal the damage mechanisms, all the damage pits are examined by a scanning electron microscope (SEM, Zeiss Auriga S40) that is equipped with a focused ion beam (FIB). The weak contrast between Al_2O_3 and SiO_2 in the SEM morphology is due to the adjacent atomic number between silicon and aluminum. The turning point of the damage probability curve for the Al_2O_3/SiO_2 mirror is around 17.0 J/cm^2. Below such fluence, typical damage pits induced by the nano-absorbing precursors are found on the surface of the Al_2O_3/SiO_2 mirror, as shown in Figs. 4(a)–4(c). Above 17.0 J/cm^2, damage initiated by the submicrometer nodular defect is found in Fig. 4(d) and the damage delamination caused by the union of multiple defects is observed at the higher fluence in Fig. 4(e). There are also many survived submicrometer nodular defects in the irradiated region, as shown in Fig. 4(f). The formation mechanism of the damage pit in Fig. 4(a) is much more like the first kind of flat bottom pit described by Dijon *et al.* [23]. The brittle fracture in the peripheral region indicates the buckling of the capping layer and only the layer just above the defect center is softened due to thermal conduction. In addition, the melted and evaporated material around the defect center is small. Therefore, the formation process of such a damage pit can be described as follows: (1) the defect absorbed laser fluence and melted the surrounding material; (2) the adhesion strength of the interface was relatively weak so that the initial crack can be easily produced, when the stress induced by the thermal expanding of the melted material reached the Griffith criterion; (3) the heated capping layer in the debonding region was buckled under the compressive stress from the surrounding cold material until the critical stress at the edge of the buckling layer was reached [23]. In principle, the critical stress of the buckling layer can be calculated with the damage depth and radius if the Young's modulus and the Poisson's ratio of the capping layer are measured. The damage pit in Fig. 4(b) is both small and shallow, which is a result of the movement of the molten front near the free surface, as illustrated by the experiment of gold nanoparticle [24]. In Fig. 4(c), the filamentous residues in the peripheral region of the damage pit indicate the thermal explosion during laser irradiation. In addition, abundant vaporized materials on the bottom of the damage pit indicate the ionization of the transparent matrix surrounding the initiator, which is the result of the temperature-activated absorption and the movement of laser-supported solid-state absorption fronts [25]. Such processes require stronger local interface adhesion to maintain sufficient duration for the laser deposition of the ionization material. The damage sources in Figs. 4(a)–4(c) are nano-absorbing precursors, which do not break the multilayer structure and are sensitive to the SWEF. The different damage morphologies induced by these nano-absorbing precursors are related to the location of the precursor and the local mechanical properties of the interface. Such defects can induce damage easily in the lower fluence, while the structural defects can endure much higher fluence. The classification of the defects here supports the defect ensemble assumption in fitting the damage probability of the Al_2O_3/SiO_2 mirror.

Although various morphologies are observed in the Al_2O_3/SiO_2 mirror, only the damage induced by the nodular ejection is found in the *double stack*, as shown in Fig. 5. The damage induced by the nano-absorbing precursors is suppressed, which is the result of the higher LIDT of fluorides as well as the extremely low electric field in oxides, as shown in Fig. 2. The damage feature difference between the Al_2O_3/SiO_2 mirror and the *double stack* again supports the assumption of the double-defect ensemble in Fig. 3. Nevertheless, three different damage morphologies are found to result from the same kind of nodular defect originating from the Al_2O_3/SiO_2 stack. Figure 5(a) depicts a flat bottom pit which forms on the interface between fluorides and oxides when the mirror is irradiated by the near LIDT laser. According to the corresponding FIB cross section, the nodular defect does not totally eject out even though the fracture along the nodular boundary is clear, which indicates that the adhesion strength between the fluorides and oxides is much more important than that of the boundary fracture around the nodular defect. In Fig. 5(b), half of the damage pit is a flat bottom pit while the other half just shows the surface ablation. As seen from the FIB cross section, there is a big survived nodular, while the half with the flat bottom pit is induced by the ejection of the small defect on the right of the survived nodular. The interface fracture between the fluorides and oxides is very clear on the left of the survived nodular, which can predict the initial formation process of the flat bottom pit. However, due to the asymmetry mechanical property around
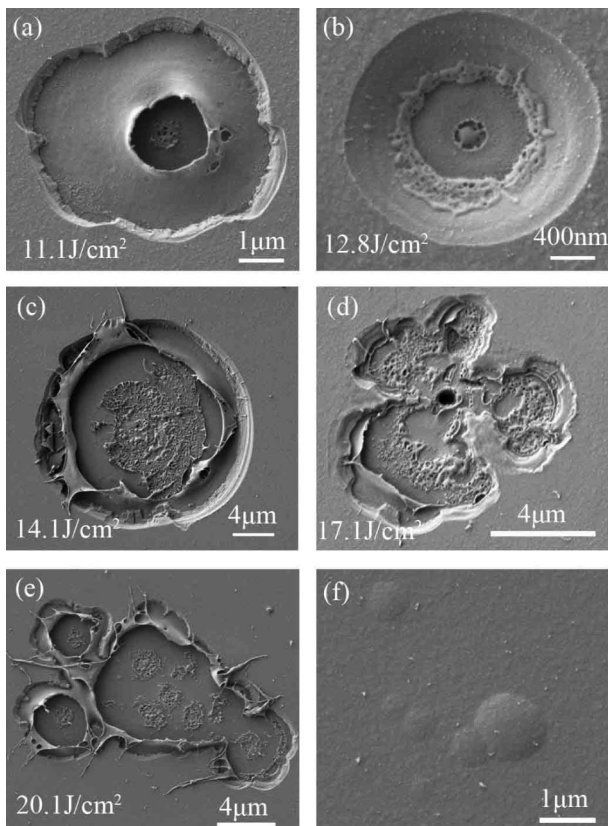

Fig. 4. SEM morphologies of the damage pits on the Al_2O_3/SiO_2 mirror.
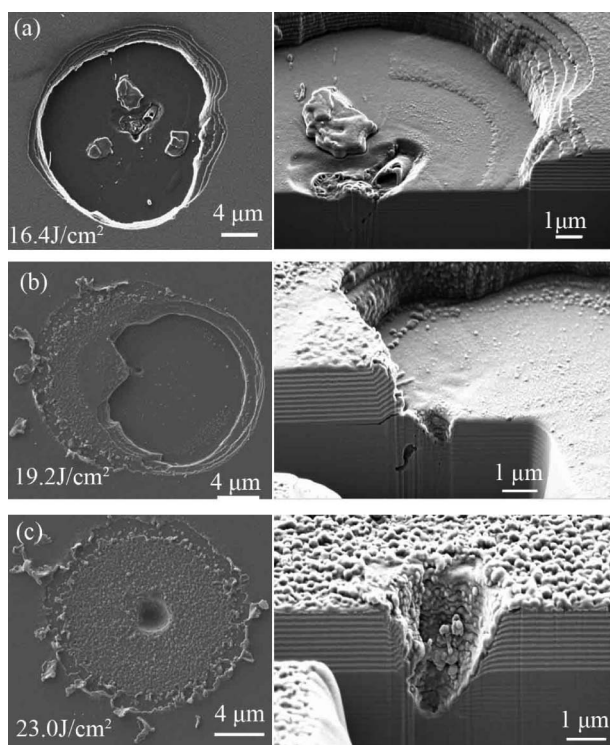
Fig. 5. SEM morphologies and the corresponding FIB cross section of the damage pits on the *double stack*.

the survived nodular defect, the ejection of the small nodular defect releases the energy and relieves the fracture propagation along the interface between the fluorides and oxides. However, under the condition of higher laser fluence and two nodular defects, the incomplete flat bottom pit indicates a much stronger adhesion strength between the fluorides and oxides at the irradiated location. In Fig. 5(c), the flat bottom pit disappears and leaves a circular ablation surface around the ejection of the nodular defect. The absence of the interface fracture indicates good adhesion strength between the fluorides and oxides, which eventually leads to the high laser resistance of such nodular defects. Studies about how the nodular defect breaks the SWEF and leads to the enhancement of the electric field have been reported by many researchers in the field of 1ω multilayer dielectric coatings [26–30]. The high LIDT of the nodular defect is not surprising and was reported in many past works. The damage features of the *double stack* indicate that the submicrometer nodular defect plays an important role in the damage process of the 3ω mirror. In the *double stack*, the local adhesion strength between the fluorides and oxides is very important to protect the nodular defect from inducing damage of the 3ω mirror. The investigations of damage mechanisms for the *double stack* encourage us to further optimize the deposition technique of the Al_2O_3/SiO_2 stack so that the nodular seed can be decreased and the adhesion strength between fluorides and oxides can be stronger in our future work.

In summary, damage precursors are classified into nanoabsorbing precursors and submicrometer nodular defects according to the shape of the damage probability curve or morphologies. The former is sensitive to the SWEF and vulnerable to irradiation, whereas the latter is related to nodule and adhesion strength between fluorides and oxides. The *double stack*

design obtained a higher LIDT after suppressing the former efficiently. The current results indicate the importance of nodular defects in oxides and the interface strength between fluorides and oxides, which direct the future process optimization to further improve the LIDT of 3ω mirrors. Depositing Al_2O_3 from metal or preparing a mixture between fluorides and oxides to improve interface strength might be our future work.

REFERENCES

1. R. Chow, M. R. Kozlowski, G. E. Loomis, and F. Rainer, Proc. SPIE **1848**, 312 (1993).
2. D. Hu, J. Dong, D. Xu, X. Huang, W. Zhou, X. Tian, D. Zhou, H. Guo, W. Zhong, X. Deng, Q. Zhu, and W. Zheng, Chin. Opt. Lett. **13**, 041406 (2015).
3. P. J. Wegner, J. M. Auerbach, T. A. Biesiada, Jr., S. N. Dixit, J. K. Lawson, J. A. Menapace, T. G. Parham, D. W. Swift, P. K. Whitman, and W. H. Williams, Proc. SPIE **5341**, 180 (2004).
4. L. Lamaignère, S. Reyne, M. Loiseau, J.-C. Poncetta, and H. Bercegol, Proc. SPIE **6720**, 67200F (2007).
5. M. Guardalben and L. Waxer, Proc. SPIE **7916**, 79160G (2011).
6. L. Yan, C. Wei, D. Li, G. Hu, K. Yi, and Z. Fan, Appl. Opt. **51**, 3243 (2012).
7. T. Izawa, N. Yamamura, R. Uchimura, S. Kimura, and T. Yakuoh, Proc. SPIE **1848**, 322 (1993).
8. Z. Czigany, M. Adamik, and N. Kaiser, Thin Solid Films **312**, 176 (1998).
9. X. Li, W. Zhang, J. Sun, Y. Hou, W. Liu, K. He, C. Wei, and K. Yi, Opt. Laser Technol. **49**, 13 (2013).
10. M. L. Grilli, F. Menchini, A. Piegari, D. Alderighi, G. Toci, and M. Vannini, Thin Solid Films **517**, 1731 (2009).
11. H. Yu, L. Wu, C. Liu, J. Shao, and Z. Fan, Opt. Laser Technol. **44**, 810 (2012).
12. X. Li, J. Liu, Y. Hou, K. He, W. Zhang, and K. Yi, Appl. Surf. Sci. **280**, 772 (2013).
13. Z. Yu, H. He, W. Sun, H. Qi, M. Yang, Q. Xiao, and M. Zhu, Opt. Lett. **38**, 4308 (2013).
14. J. Liu, W. Zhang, H. Cui, J. Sun, H. Li, K. Yi, and M. Zhu, Chin. Opt. Lett. **12**, 083101 (2014).
15. H. Wang, H. Qi, B. Wang, Y. Cui, M. Guo, J. Zhao, Y. Jin, and J. Shao, Opt. Express **23**, 5213 (2015).
16. J. Bude, P. Miller, S. Baxamusa, N. Shen, T. Laurence, W. Steele, T. Suratwala, L. Wong, W. Carr, D. Cross, and M. Monticelli, Opt. Express **22**, 5839 (2014).
17. S. Baxamusa, P. Miller, L. Wong, R. Steele, N. Shen, and J. Bude, Opt. Express **22**, 29568 (2014).
18. W. Liu, C. Wei, K. Yi, and J. Shao, Chin. Opt. Lett. **13**, 041407 (2015).
19. W. Liu, C. Wei, K. Yi, and J. Shao, Chin. Opt. Lett. **13**, 1404 (2015).
20. H. A. Macleod, *Thin-Film Optical Filters*, 3rd ed. (Institute of Physics, 2001).
21. ISO21254-1, "Lasers and Laser-Related Equipment–Methods for Laser-Irradiation-Induced Damage Threshold–Part 1: Definitions and General Principles" (2011).
22. H. Krol, L. Gallais, C. Grezes-Besset, J.-Y. Natoli, and M. Commandre, Opt. Commun. **256**, 184 (2005).
23. J. Dijon, G. Ravel, and B. Andre, Proc. SPIE **3578**, 398 (1999).
24. S. Papernov and A. Schmid, Proc. SPIE **7132**, 71321J (2008).
25. C. Carr, J. Bude, and P. DeMange, Phys. Rev. B **82**, 184304 (2010).
26. C. J. Stolz, M. D. Feit, and T. V. Pistor, Appl. Opt. **45**, 1594 (2006).
27. C. J. Stolz, S. Hafeman, and T. V. Pistor, Appl. Opt. **47**, C162 (2008).
28. L. Smalakys, G. Batavičiūtė, E. Pupka, and A. Melninkaitis, Proc. SPIE **9237**, 92371I (2014).
29. L. Gallais, X. Cheng, and Z. Wang, Opt. Lett. **39**, 1545 (2014).
30. X. Cheng, A. Tuniyazi, Z. Wei, J. Zhang, T. Ding, H. Jiao, B. Ma, H. Li, T. Li, and Z. Wang, Opt. Express **23**, 8609 (2015).